Petroleum Science 21 (2024) 1257–1274

Contents lists available at ScienceDirect

Petroleum Science

journal homepage: www.keaipublishing.com/en/journals/petroleum-science

Original Paper

Experimental and numerical simulation study on the erosion behavior of the elbow of gathering pipeline in shale gas field

En-Bin Liu [a, *], Shen Huang [a], Ding-Chao Tian [a, b], Lai-Min Shi [c], Shan-Bi Peng [d, e, **], He Zheng [f]

[a] Petroleum Engineering School, Southwest Petroleum University, Chengdu 610500, Sichuan, China
[b] Chongqing Natural Gas Sales Center, Natural Gas Branch, Sinopec, Chongqing, 400023, China
[c] Zhejiang Zheneng Natural Gas Operation Co., Ltd., Hangzhou 310000, Zhejiang, China
[d] School of Civil Engineering and Architecture, Southwest Petroleum University, Chengdu 610500, Sichuan, China
[e] Louisiana Tech Univ, Trenchless Technol Ctr, 599 Dan Reneau Dr, Ruston, LA, 71270, USA
[f] Southwest Oil and Gas Field Branch Natural Gas Research Institute, Chengdu 610213, Sichuan, China

ARTICLE INFO

Article history:
Received 30 January 2023
Received in revised form
17 May 2023
Accepted 29 August 2023
Available online 30 August 2023

Edited by Jia-Jia Fei and Min Li

Keywords:
Shale gas
Gas gathering pipeline
Elbow
Erosion
CFD

ABSTRACT

During the production period of shale gas, proppant particles and rock debris are produced together, which will seriously erode the elbows of gathering pipelines. In response to this problem, this paper takes the elbow of the gathering pipeline in the Changning Shale Gas Field as an example to test the erosion rate and material removal mechanism of the test piece at different angles of the elbow through experiments and compares the four erosion models with the experimental results. Through analysis, it is found that the best prediction model for quartz sand-carbon steel erosion is the Oka model. Based on the Oka model, FLUENT software was used to simulate and analyze the law of erosion of the elbow of the gas gathering pipeline under different gas flow velocities, gas gathering pressure, particle size, length of L1, and bending directions of the elbow. And a spiral pipeline structure is proposed to reduce the erosion rate of the elbow under the same working conditions. The results show that this structure can reduce erosion by 34%.

1. Introduction

In recent years, in the face of unreasonable energy structure and increasing energy dependence, China has vigorously developed shale gas exploitation and achieved an annual output of 20 billion cubic meters in less than 10 years (Liu et al., 2019). Shale gas exploitation is different from that of conventional gas, which requires hydraulic fracturing, with high pressure and high sand yield in the initial stage of exploitation (Peng et al., 2019). As a weak link in the pipeline, the elbow compared with other components bears the high-speed impact of solid sand in addition to internal pressure and medium corrosion, so its erosive wear is more serious (Peng et al., 2020a). According to existing experience and data, the rate of erosive wear of the elbow is more than 50 times greater than that of the straight pipe part. Therefore, it is of great practical significance to study gas-solid two-phase flow in shale gas gathering and transportation pipelines and reveal its erosion mechanism.

Various factors influence the erosion, involving material properties and stress loading of the target material, particle size, particle shape, particle hardness, particle impact velocity and angle, particle concentration, fluid properties, etc. (Arabnejad et al., 2015; Islam et al., 2016; Yang et al., 2021; Yi et al., 2021). Some scholars have adopted experimental research methods for erosion wear caused by particles, as shown in Table 1. It can be seen that early scholars such as Levy (1981) and Yabuki et al. (1999) mainly considered the influence of the properties of the eroded material and solid particles on erosion, without discussing key parameters such as particle impact angle. With the deepening of research and the updating of experimental equipment, scholars have begun to pay attention to the impact angle on erosion, and have revealed the wear morphology and erosion mechanism of stainless steel at different impact angles. Khan et al. (2019) also visualized the erosion of the inner wall of the elbow by cutting the elbow. However, there are

* Corresponding author.
** Corresponding author.
E-mail address: sunriselebpsb@163.com (E.-B. Liu).

https://doi.org/10.1016/j.petsci.2023.08.034

Table 1
Experimental-based on experiments.

Experimental facility	Results and conclusions	Reference
Blast tester	By changing the pressure and airflow, and then changing the particle velocity, we conclude that the hardness of different tissues is inversely proportional to the erosion rate.	Levy (1981)
Rotating target device	The critical impact velocity for particle impact depends on the hardness of the material and particles, as well as the shape and size of the solid particles.	Yabuki et al. (1999)
Sandblaster	The relationship between erosion rate and impact angle shows three obvious wear areas under the different material hardness.	Rodriguez et al. (2009)
The new type of wind and sand erosion test machine	The influence of impact angle and test time on the high-speed erosion of stainless steel is studied, and the erosion characteristics and behavior of stainless steel samples are revealed.	Nguyen et al. (2014)
Multi-phase flow circulation meter	Cut 90° elbows to visualize the corrosion inside the elbow and calculate the erosion rate of the elbow by mass loss.	Khan et al. (2019)
The jet impingement apparatus for erosion-corrosion	The erosion-corrosion of stainless steel 304 at a low impact angle is a micro-cutting mechanism, and when the impact angle increases to 60° and 90°, it is a plastic deformation mechanism.	Yi et al. (2021)
Self-made gas-solid two-phase erosion device	Erosion of the material is most severe when the particle impact angle is 30°, and 304 stainless steel and L245 carbon steel are cut at low angles, and impacted at high angles to form erosion pits.	Hong et al. (2022)

limitations in using experiments alone to reveal the mechanism of erosion, a complex phenomenon with multiple influencing factors, and it is difficult to fully describe the erosion process under a single condition. With the development of modern science and technology and related theories, computational fluid mechanics (CFD) is widely used to predict particle erosion, as shown in Table 2. FLUENT software provides users with Generic, Finnie, McLaury, and Oka erosion prediction models, which can calculate the movement track of particles and erosion rate, and conduct qualitative and quantitative analysis.

As can be seen from Table 2, many researchers have studied the erosion behavior of particles using the erosion model in FLUENT, however, some scholars only considered the particle-wall collisions and neglected the interactions between particles, while Sun and Cao (2021) investigated this and found that the collisions of particles affect their motion paths and erosion rates. Some scholars also validated the reliability of the models used in the paper, Farokhipour et al. (2019) verified the reliability of the turbulence model as well as the bounce and erosion models by comparing them with the available experimental data. Tofighian et al. (2020) determined the most accurate model applicable to the conditions in the paper by comparing different diffusion models and particle-wall collision models. However, most of the erosion models used in these studies are summarized under specific conditions and are not applicable to all erosion situations. Therefore, in order to be closer to the field conditions, this paper will conduct experiments based on the field conditions and select the most applicable erosion model to analyze the erosion influencing factors.

The second part of this paper proposes experimental conditions and builds a simplified experimental setup based on the site conditions of the Changning Shale Gas Field in Sichuan, China. In the third part, the physical model of the pipeline and the mathematical model for calculating the erosion rate is established according to the working parameters of the field research. The fourth part selects the optimal erosion model based on the comparison between the analysis by the FLUENT fluid software and the experimental results and analyzes the law of erosion of the pipe elbow under different influence conditions. In the fifth part, the elbow erosion improvement scheme is proposed based on the simulation analysis results and verified by numerical simulation.

2. Experimental research and numerical methods

2.1. Experimental method

2.1.1. Experimental materials

The erosion target in this experiment is a 20# carbon steel elbow with an outside diameter of 89 mm and a bending to diameter ratio of 1.5. The chemical composition of 20# carbon steel is shown in Table 3. In order to observe the erosion area of the elbow more accurately, we conducted a pre-erosion experiment before the formal experiment and prepared a sample of the elbow for each of the two experiments. In the pre-erosion test, the preparation of the elbow specimen includes cutting, grinding and

Table 3
Chemical composition of 20# steel.

C	Si	Mn	S	P	Cr	Ni	Cu
17–0.24	17–0.37	0.35–0.65	≤0.35	≤0.035	≤0.25	≤0.25	≤0.25

Table 2
Research on erosion behavior based on numerical simulation.

Research object	Research contents	Reference
Liquid-solid two-phase flow, straight pipe section	The CFD code was modified to take into account the effect of particle size on the area of particle impact near the wall.	Zhang et al. (2009)
Liquid-solid two-phase flow, pump	The discrete phase model (DPM) is used to obtain the dilute slurry flow field within the pump, and the standard k-ε model is used for turbulence.	Pagalthivarthi et al. (2011)
Gas-solid two-phase flow, throttle valve	Prediction of throttle mass loss and erosion distribution using the discrete phase model (DPM) and the semi-empirical material removal model.	Fu and Wang (2015)
Gas-solid two-phase flow, three-way gas collection pipeline	The reliability of the selected turbulence model and the E/CRC erosion model was verified by comparing them with the available experimental data, and the validated model was used to simulate gas-solid two-phase flow at different velocities and mass loads.	Farokhipour et al. (2019)
Gas-solid two-phase flow, cyclone separator	Comparison of accuracy of separation efficiency and erosion rate of cyclone separators simulated by different diffusion models and particle wall collision models.	Tofighian et al. (2020)
Gas-solid two-phase flow, elbow	The DSMC method is used to consider the collision behavior between the particles, and it is found that the maximum erosion position of the bend is shifted. The research shows that the collision of particles can affect their movement path and erosion rate.	Sun and Cao (2021)

painting. The cutting method is shown in Fig. 1. After the elbow was divided into two parts by the cutter, the elbow was sanded and polished using sandpaper. To facilitate the observation of the erosion area, paint with weak adhesion was applied to the inner wall of the elbow. After the sample preparation, we conducted a 4-h pre-erosion experiment, and the experimental results are shown in Fig. 2.

It can be seen from Fig. 2 that the main erosion area is located at 50°–70° of the paint surface outside the elbow (0° at the entrance), the width of the erosion area is about 30 mm, and the paint surface inside the elbow has no change. Based on this, it is inferred that under the experimental conditions, the inner sidewall of the elbow is hardly affected by erosion. After specifying the main erosion position of the elbow, the cutting scheme of the elbow specimen in the formal experiment is determined as follows: On the outside of the elbow, cut the pipe wall with a width of about 30 mm along the arc trajectory, and then cut the cut pipe wall into 9 test pieces, as is shown in Fig. 3. Wire cutting is adopted as the cutting method, and the cutting loss is about 0.2 mm, which has little influence on the geometric shape of the sample and thus can be ignored.

In the actual production process of shale gas well site, the extraction of proppant particles is the main factor causing the erosion of the gas collection pipeline at the wellhead, so in the experiments of this paper, the sand particles are selected from 40 to 70 mesh fracturing proppant commonly used in shale gas sites in order to meet the actual situation in the field, and their scanning electron microscope images are shown in Fig. 4. It can be seen that the geometry of the ceramic proppant is close to round, without sharp edges, and the particle size difference is small.

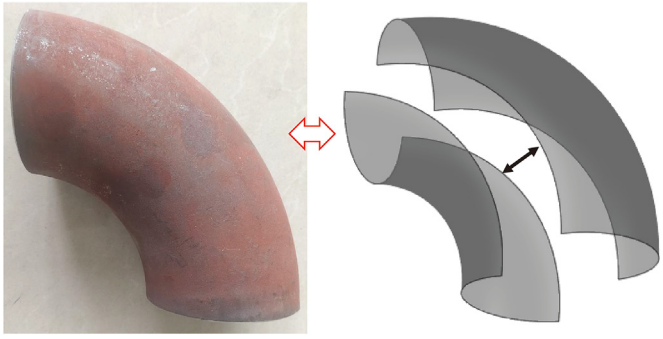

Fig. 1. Pre-erosion test elbow cutting method.

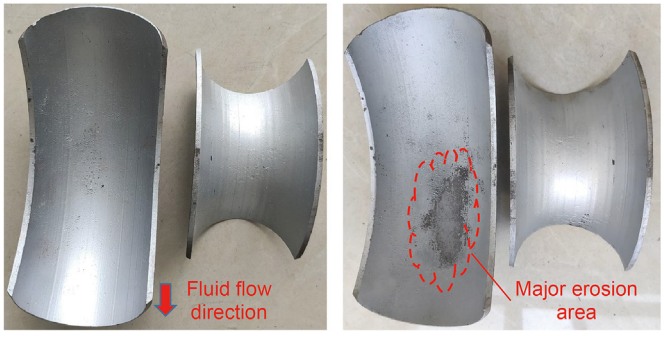

Fig. 2. Pre-erosion test results.

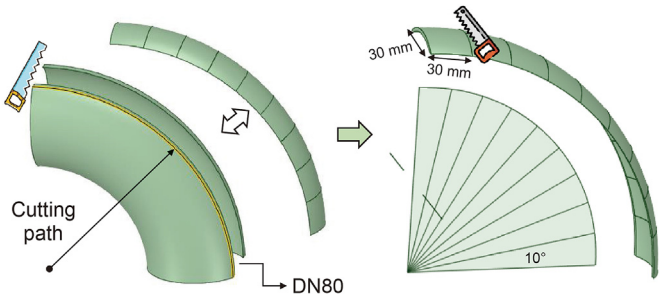

Fig. 3. Schematic diagram of test piece cutting.

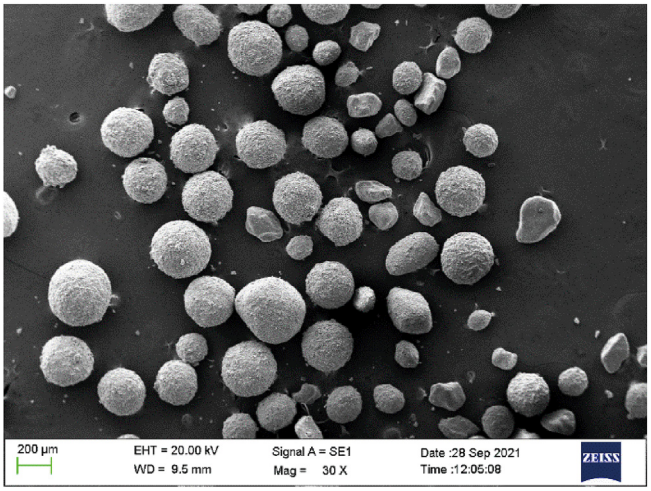

Fig. 4. 40–70 mesh vitrified proppant 500x scanning electron micrograph.

2.1.2. Experimental set-up

In this study, the gas-solid two-phase erosion experimental device shown in Fig. 5 is established, with a size of 2500 mm × 500 mm × 2200 mm, which consists of an air supply device, feeding device, flowmeter, main pipeline, sample, and clamping device. Among them, the air supply device is a variable frequency fan with a maximum airflow supply of 60 m^3/min. The flow meter is a vortex flowmeter with a backup orifice set 20 cm downstream of the flowmeter for flow rate measurement. In this experiment, the airflow velocity is controlled at 12 m/s according to the field conditions. The sand feeding device is a screw feeder, the screw diameter of the device is 38 mm, and the feeding flow is 2–6 kg/h. Considering that the experiment will be carried out for a long time, if the experimental flow differs greatly from the rated flow of the feeding device, it is not suitable for stable work for a long time, so the feeding device flow is fixed as the rated flow, which is calculated as 5.2 kg/h according to the test. The elbow specimen clamping device is customized with polyurethane material and cast with an 89 mm outside diameter elbow, thus achieving a complete fit with the elbow.

2.1.3. Experimental process

In this study, the erosion rate and material removal mechanism of the elbow were characterized by the weightlessness method and scanning electron microscope respectively. The erosion rate is calculated by the following formula:

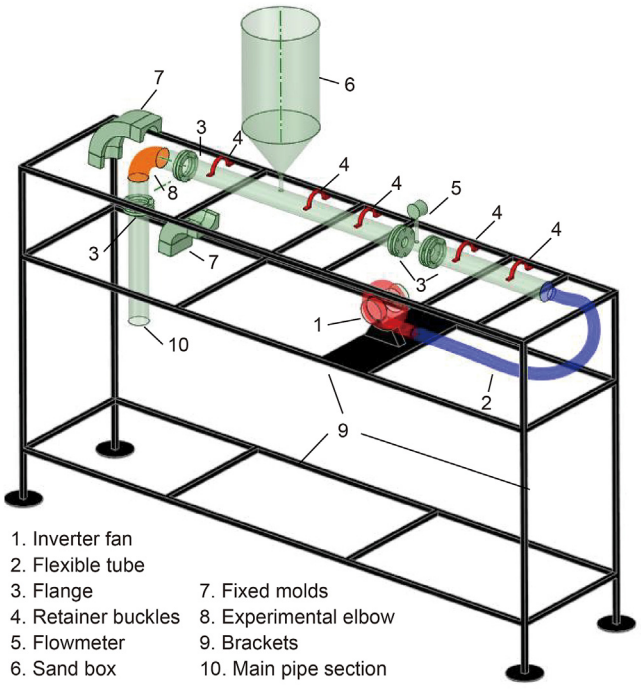

Fig. 5. Experimental setup for gas-solid two-phase flow erosion.

$$ER = \frac{1}{3600000} \times \frac{w_0 - w_1}{S \cdot t \cdot \rho_w} \tag{1}$$

where w_0 is the mass of the test piece before the experiment, w_1 is the weight of the test piece after the experiment, S is the eroded area of the test piece surface, t is the time the experiment was conducted, and ρ_w is the density of the test piece material.

In order to ensure the reliability of the experimental results, four experiments were carried out in this paper. Finally, the effective test data were selected and the average value was taken to calculate the erosion rate. In the experiment, the weight of the test piece was recorded every 24 h and the experiment lasted for 7 days. The specific steps of the experiment are as follows:

(1) The first step is to pretreat the test piece. Before the start of the experiment, the test pieces were polished with sandpaper first, then the surface of the test pieces was cleaned with aqueous ethanol, and the wind swept. Finally, the high-precision analytical balance was used for weighing.
(2) The second step is to assemble the test piece. Place the test piece and check the orientation of the elbow and the arrangement of the test piece.
(3) The third step is equipment inspection. Check the integrity and air tightness of the power supply and pipes to ensure that the hose is unblocked and that there is enough sand left in the sandbox.
(4) Step three begins the experiment. Open the fan, adjust the wind speed with the anemometer, and make it stable; turn on the sand feeder and record the start time of the experiment. After the experiment, shut down the device and record the end time of the experiment.
(5) The fifth step is to process the test piece. Open the mold, take off the test piece, purge the test piece with an airbrush, clean and air dry with aqueous ethanol, and finally weigh the test piece and record the result.
(6) After completing the above steps, a scanning electron microscope was used to observe the surface of the test piece and analyze the material removal mechanism.

2.2. Mathematical model

2.2.1. Gas-phase governing equation

There are two kinds of continuous phase governing equations, Model A and Model B, in CFD. Among them, Model A believes that the pressure drop is the result of the combined action of gas and particles, while Model B believes that the pressure drop is only determined by the flow of gas. The gas-particle two-phase flow can be viewed as a simplified version of Model A in this paper. The summary of Model A is as follows (Parvaz et al., 2018):

Continuity equation:

$$\frac{\partial}{\partial t}\left(\varepsilon_g \rho_g\right) + \frac{\partial\left(\varepsilon_g \rho_g u_{g,i}\right)}{\partial x_i} = 0 \tag{2}$$

Momentum conservation equation:

$$\frac{\partial}{\partial t}\left(\varepsilon_g \rho_g u_{g,i}\right) + \frac{\partial}{\partial x_j}\left(\varepsilon_g \rho_g u_{g,i} u_{g,j}\right) = -\varepsilon_g \frac{\partial p}{\partial x_i} + \frac{\partial}{\partial x_j}\left(\varepsilon_g \tau_{g,ij}\right) - S + \varepsilon_g \rho_g g_i \tag{3}$$

where ε_g is the porosity; ρ_g is the gas density; p is the gas pressure; u_g is the gas velocity; τ_g is the gas viscosity; g_i is the acceleration of gravity; S is the momentum source term.

2.2.2. Discrete phase model(DPM)

The research object of this paper is the gas-solid two-phase erosion process of gas gathering pipeline, and the particle load is low (with a mass ratio less than 5%). Therefore, the DPM is used for numerical simulation.

The force balance equation of discrete phase particles in the x-direction in the Cartesian coordinate system is in the form of (Haider and Levenspiel, 1989):

$$\frac{du_p}{dt} = F_D\left(u - u_p\right) + \frac{g_x\left(\rho_p - \rho\right)}{\rho_p} + F_x \tag{4}$$

where $F_D(u - u_p)$ is the drag force of particles per unit mass. F_D can be expressed as:

$$F_D = \frac{18\mu}{\rho_p d_p^2}\frac{C_D Re}{24} \tag{5}$$

where u is the gas flow rate, u_p is the particle impact rate, μ is the gas dynamic viscosity, ρ is the gas density, ρ_p is the density of solids, d_p is the solid particle size, Re is the relative Reynolds number, which is calculated by the following formula:

$$Re = \frac{\rho d_P |u_P - u|}{\mu} \tag{6}$$

C_D is the drag coefficient, and its expression is as follows:

$$C_D = a_1 + \frac{a_2}{Re} + \frac{a_3}{Re^2} \tag{7}$$

For spherical particles, within a certain range of Reynolds numbers, a_1, a_2, a_3 are constants (Jassim et al., 2010).

Particle diameter distribution of solid particles obtained from on-site shale gas field conforms to R–R distribution, and its solid particle diameter distribution function is expressed as follows:

$$F(d) = 1 - \exp\left[-\left(\frac{d}{d_{50}}\right)^m\right] \tag{8}$$

where d is the particle size; d_{50} is the median particle diameter, which is 300 μm in this paper; m is the distribution range index, which is 3.5 in this paper.

2.2.3. Turbulence model

This paper adopts the Realizable k-ε turbulence model and uses the standard wall function. The governing equation is as follows:

$$\frac{\partial(\rho k)}{\partial t} + \frac{\partial(\rho k u_i)}{\partial x_i} = \frac{\partial}{\partial x_j}\left[\left(\mu + \frac{\mu_t}{\sigma_k}\right)\frac{\partial k}{\partial x_j}\right] + G_k + G_b - \rho\varepsilon - Y_M + S_k \tag{9}$$

$$\frac{\partial(\rho\varepsilon)}{\partial t} + \frac{\partial(\rho\varepsilon u_j)}{\partial x_j} = \frac{\partial}{\partial x_j}\left[\times\left(\mu + \frac{\mu_t}{\sigma_\varepsilon}\right)\frac{\partial \varepsilon}{\partial x_j}\right] + \rho C_1 S_\varepsilon - \rho C_2 \frac{\varepsilon^2}{k + \sqrt{\nu\varepsilon}} + C_{1\varepsilon}\frac{\varepsilon}{k}C_{3\varepsilon}G_b + S_\varepsilon \tag{10}$$

The formula for turbulent viscosity, denoted by k and ε, is as follows :

$$\mu_t = \rho C_\mu \frac{k^2}{\varepsilon} \tag{11}$$

To better consider the rotation effect, C_μ is no longer a constant, but a function related to the average shear rate, and the function C_μ is expressed in the following equation:

$$C_\mu = \frac{1}{A_0 + A_s U^* \frac{k}{\varepsilon}} \tag{12}$$

In the formula, $U^* = \sqrt{S_{ij}S_{ij} + \Omega^*_{ij}\Omega^*_{ij}}$, $\Omega^*_{ij} = \Omega_{ij} - 2\varepsilon_{ijk}\omega_k$, $\Omega_{ij} = \overline{\Omega}_{ij} - 2\varepsilon_{ijk}\omega_k$, $A_0 = 4.04$, $A_s = \sqrt{6}\cos\varphi$, where $\overline{\Omega}_{ij}$ is the is the time-averaged rotational rate observed from a reference frame with angular velocity ω_k.

2.2.4. Oka erosion model and particle-wall rebound model

The Oka erosion model (Oka and Nagahashi, 2003; Oka and Yoshida, 2005) can be used to simulate erosion of different materials. For example, sand-steel erosion and sand-aluminum erosion can be considered. The difference is that the material has different Vickers hardness. Many scholars believe that the Oka erosion model is highly accurate in predicting the erosion of carbon steel by sand particles (Chen et al., 2020), and its carbon steel erosion constants are shown in Table 4. Its expression is as follows:

$$E = E_{90}\left(\frac{V}{V_{ref}}\right)^{k2}\left(\frac{d}{d_{ref}}\right)^{k3} f(\gamma) \tag{13}$$

$$f(\gamma) = (\sin\gamma)^{n_1}(1 + H_v(1 - \sin\gamma))^{n_2} \tag{14}$$

where E_{90} is the erosion rate when V=V_{ref}, $d = d_{ref}$, $\gamma = 90°$; V is the relative velocity between the particle and the wall; V_{ref} is the particle reference velocity constant; d and d_{ref} are particle diameter and particle reference diameter respectively; γ is the wall impact angle; H_v is the Vickers hardness of the material; n_1 and n_2 specify constants for users.

In the computational fluid dynamics software, the rebound model of particle-wall collision is always combined with the erosion prediction model to calculate the dynamic motion of the particles, their erosion rate, and their maximum erosion position (Zhang et al., 2021). The rebound model of particle-wall collision proposed by Grant and Tabakoff (1975) and Forder et al. (1998) was used together with the erosion prediction model to study the particle trajectory and calculate the impact and erosion of particles on the wall. The model proposed by Forder et al. is as follows (Forder et al., 1998):

$$\varepsilon_n = 0.998 - 0.78\theta + 0.19\theta^2 - 0.024\theta^3 + 0.027\theta^4 \tag{15}$$

$$\varepsilon_t = 1 - 0.78\theta + 0.84\theta^2 - 0.021\theta^3 + 0.028\theta^4 - 0.022\theta^5 \tag{16}$$

The model proposed by Grant and Tabakoff is as follows (Grant and Tabakoff, 1975) :

$$\varepsilon_n = 0.993 - 1.76\theta + 1.56\theta^2 - 0.49\theta^3 \tag{17}$$

$$\varepsilon_t = 0.998 - 1.66\theta + 2.11\theta^2 - 0.67\theta^3 \tag{18}$$

where θ is the particle incidence angle.

2.3. Physical model and boundary conditions

To meet the site production conditions, the commonly used

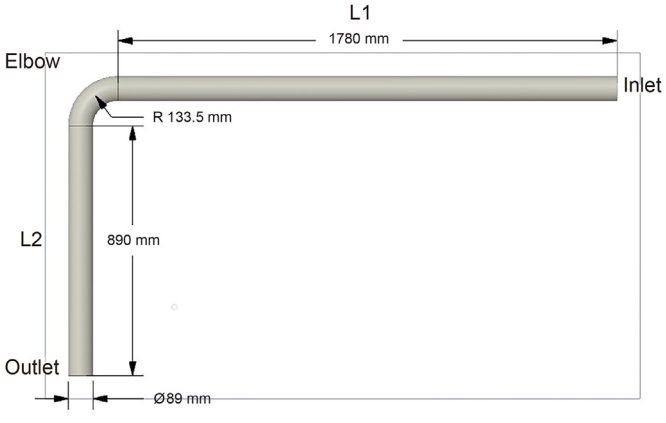

Fig. 6. Pipeline geometric model.

Table 4
Oka erosion model constant.

Constant	E_{90}	H_v	n_1	n_2	k_2	k_3	d_{ref}	V_{ref}
Sand-carbon steel	6.154e^{-4}	1.8 GPa	0.8	1.3	2.35	0.19	326 μm	104 m/s

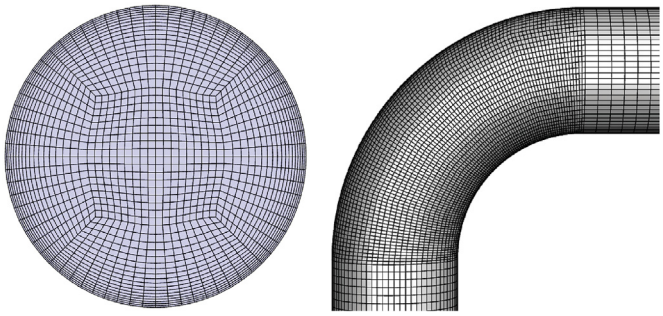

Fig. 7. Schematic diagram of grid refinement (**a**) cross-section grid node distribution (**b**) elbow mesh encryption.

Table 5

Grid number	1003722	1502732	2767784	3710828	4415696
Velocity, m/s	8.125618	8.131595	8.188635	8.188685	8.188615

specification pipeline in the Changning Shale Gas Field was selected, with a pipeline diameter of 89 mm and an elbow bend diameter ratio of R/D = 1.5. To exclude as much as possible the influence of the flow field and particle injection method on the simulation results, the length of L1 was extended as much as possible (Liu et al., 2021a), and the length of L1 was 20 D and the length of L2 was 10 D, which can be seen in Fig. 6.

In this paper, the geometric model in Fig. 6 is divided into structured meshes, and the meshes in the elbow area are encrypted. The grid at the pipe section and elbow is shown in Fig. 7, where the thickness of the first boundary layer is set as the maximum particle size, which is conducive to obtaining good erosion prediction results. Then, under the same parameter conditions, the maximum velocity value of the straight pipe section before the elbow is extracted to verify the mesh independence of the pipe elbow model. As is shown in Table 5, when the number of grids reaches 2767784, with the increase of the number of grids, the velocity value changes less, only 0.00001 m/s. To take into account calculation accuracy and calculation efficiency, this paper selects a grid with a grid number of 2767784 for the final calculation grid (Peng et al., 2020b; Liu et al., 2021b). The particles and fluid are injected uniformly at the same velocity into the inlet of the tube section and set the boundary condition here as velocity inlet and apply the pressure outlet boundary condition at the outlet, with the surface of the tube section set as a non-slip wall surface.

According to the on-site investigation of the production site, the simulated working conditions are determined as shown in Table 6. The benchmark working conditions are a gas flow rate of 8 m/s, a gathering pressure of 6 MPa, the R–R distribution of the particle size, a sand volume of 10 kg/d, a length of L1 of 20 D, and a gravity direction +Z.

3. Results and discussion

3.1. Comparative analysis of experiment and numerical simulation

3.1.1. Experimental results

Under the condition of the gas flow rate of 12 m/s and sand flow volume of 5.2 kg/h, 7 sets of experimental data are shown in Fig. 8. It can be seen that the mass loss of each test piece per 24 h first decreased and then increased with time. At the beginning of the experiment, the rusted part of the surface of the test piece was removed due to sandblasting rust removal, and the weight loss was greater at this time. Then, the weight loss became smaller when the rust was removed. As the experiment progressed, the surface Sof the sample was continuously impacted by sand particles, resulting in fatigue failure, and the mass loss continued to increase with time.

Table 6
Simulation condition settings.

Influence factors	Numerical simulation data
Gas flow rate, m/s	4, 6, 8, 10, 12, 14
Gathering pressure, MPa	4, 5, 6, 7, 8, 9
Particle size, mm	0.080, 0.096, 0.125, 0.150, 0.180, 0.212
Length of L1	20 D, 25 D, 30 D, 35 D
Gravity direction	+Y, −Y, +Z

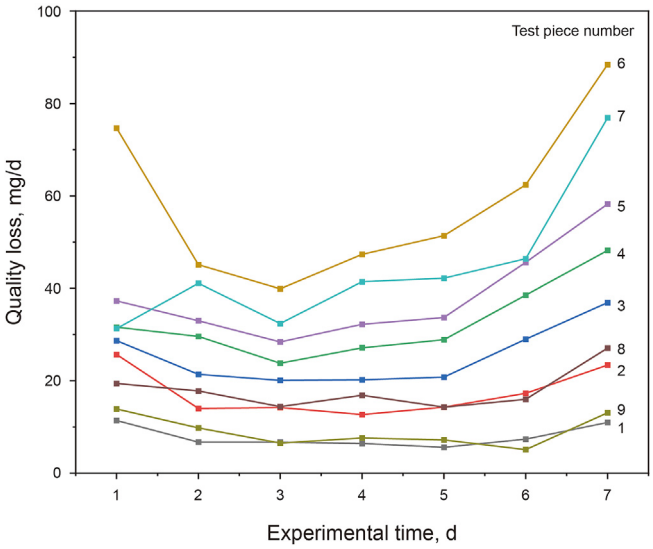

Fig. 8. Weightlessness curve of test specimens.

Fig. 9 shows the erosion morphology of the test piece under a 500x electron microscope. According to the results of scanning electron microscopy, the mass loss of test pieces 1–3 is mainly due to cutting action. With the increase of impact angle, the mass loss gradually increases, and the “furrow” caused by the cutting action gradually shortens. Test piece 4 began to take on plastic deformation and produce a “skirt”. The “furrow” of test piece 6 basically disappears, at this time the mass loss reaches the maximum, and plastic extrusion deformation becomes the main cause of material loss. With the increase of the impact angle, the “skirts” caused by plastic deformation in test pieces 7–9 continued to become denser, and the mass loss decreased instead.

3.1.2. Comparative analysis of erosion models

Fig. 10 shows the erosion rates obtained by experimental and numerical simulations. It can be seen that the variation trend of the mercury model, Finnie model, and Oka model on test pieces 1–9 is roughly the same as that of the experimental data, showing an increase first and then a decrease, and the erosion rates of test pieces 1, 2, 3 and 8, 9 are at a low level under the same model. The erosion rate under the Generic model is lower compared with that under other models and the experimental data and has little fluctuation. The erosion rate under the Mclaury model is several times of the experimental data, and the difference is large. The predicted results of the Finnie model at 0°–40° are quite different from the

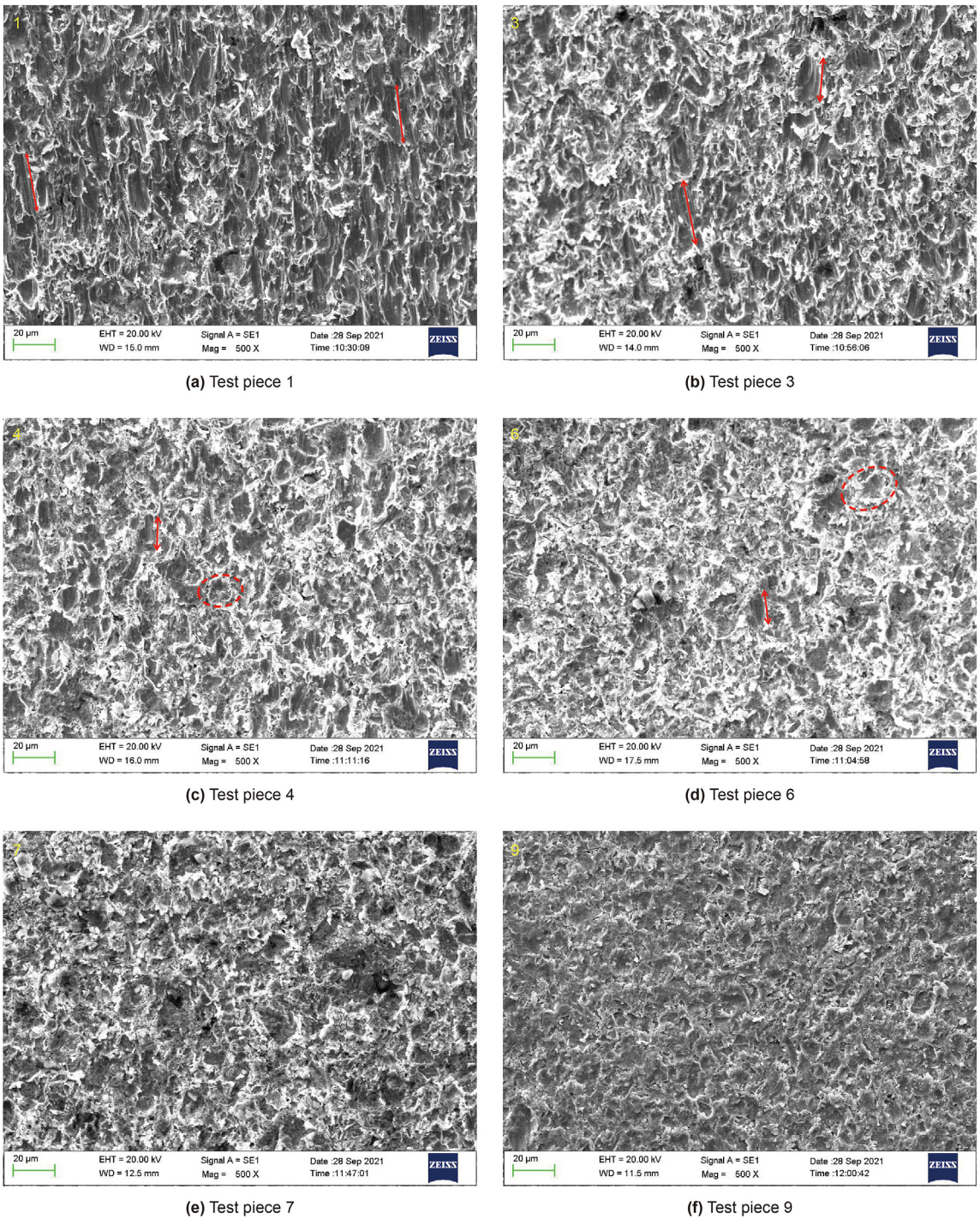

(a) Test piece 1 **(b)** Test piece 3

(c) Test piece 4 **(d)** Test piece 6

(e) Test piece 7 **(f)** Test piece 9

Fig. 9. Erosion morphology of test pieces under 500x electron microscope.

experimental data. The relative error between the Finnie model and experimental results at 50°–90° is in the range of +18%~+151%, but it is still larger than that of the Oka model. The Oka model is in better agreement with the experimental data as the prediction results only differ significantly from the experimental data at 0°–40°, and the relative error with the experimental results at 50°–90° is −11% to +18%, which has a high prediction accuracy. In addition, among these erosion models, the Mclury model is mainly used to predict the erosion rate during mud erosion. Finnie model is applicable to the case of sand impacting carbon steel wall in this paper, but the setting of its model constant is not applicable to the case in this paper. Although the Generic model is a generalized erosion model, the erosion phenomenon is not obvious in this paper. The Oka model is a more complex erosion model proposed on

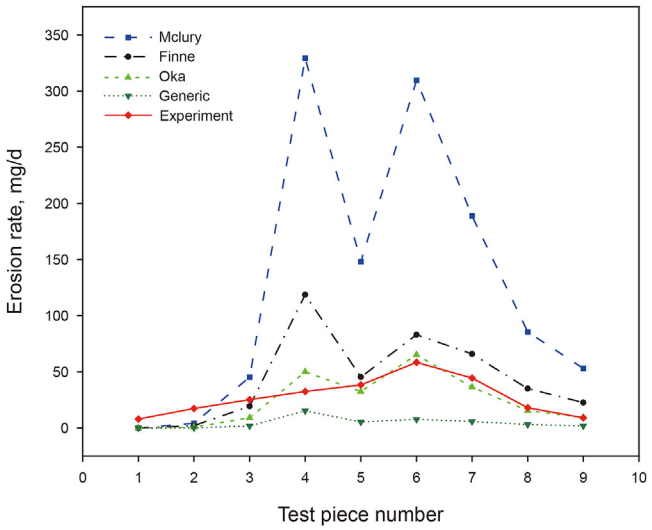

Fig. 10. Comparison of weight loss and experimental data for different erosion models.

the basis of summarizing a large number of experimental data, which considers more erosion factors than other models. In summary, the Oka model is more suitable for the working conditions in this article. Therefore, the Oka model was adopted as the erosion prediction model in subsequent simulations.

3.2. Analysis of factors influencing elbow erosion

3.2.1. Influence of gas flow rate on elbow erosion

In this section, the flow field of the pipeline is simulated when the gas flow rate is 4–14 m/s, and the erosion behavior of particles in the pipeline is analyzed, while other parameters are based on the reference conditions.

Fig. 11 is the wall erosion cloud diagram of the pipeline in the direction of the +X and +Z view, showing the influence of gas flow rate on the wall erosion rate and indicating that the maximum erosion rate increases as the inlet velocity increases. In combination with the particle track diagram (Fig. 12), when the gas flow rate is small (4–6 m/s), particle tracks are relatively clustered, and the collision between particles and L1 bottom causes more obvious erosion traces. With the increase of gas flow velocity (8–14 m/s), the particles are more widely distributed and less aggregated on the flow cross-section. The erosion in L1 region gradually weakens until disappears, and the main erosion area transfers from L1 to L2. At the same time, as the gas flow rate increases, the velocity and the angle of attack when the particles collide with the elbow wall are larger, causing more serious erosion.

Fig. 13 indicates that the maximum erosion rate of the elbow and L2 gradually increases as the gas flow rate increases, and the maximum erosion rates are 0.89×10^{-8}–4.55×10^{-8} kg/(s·m^2) and 0.52×10^{-8}–4.13×10^{-8} kg/(s·m^2), respectively. And the maximum erosion rate on L1 gradually decreases with the increase of airflow velocity, and the maximum erosion rate is 0.398×10^{-8}–1.288×10^{-8} kg/(s·m^2). Therefore, to avoid serious erosion in the elbow, the gas flow rate in the pipeline should be minimized.

As is shown in Fig. 14, nine data extraction rings were intercepted to study the erosion positions and erosion rates of different sections on the elbow wall. As is shown in Fig. 15, serious erosion is mainly concentrated in the area at 180° ± 20° on the cross-section R1–R5, and the area with maximum erosion is located at 184° on the cross-section R2 this time. There is local erosion at 120°–135°

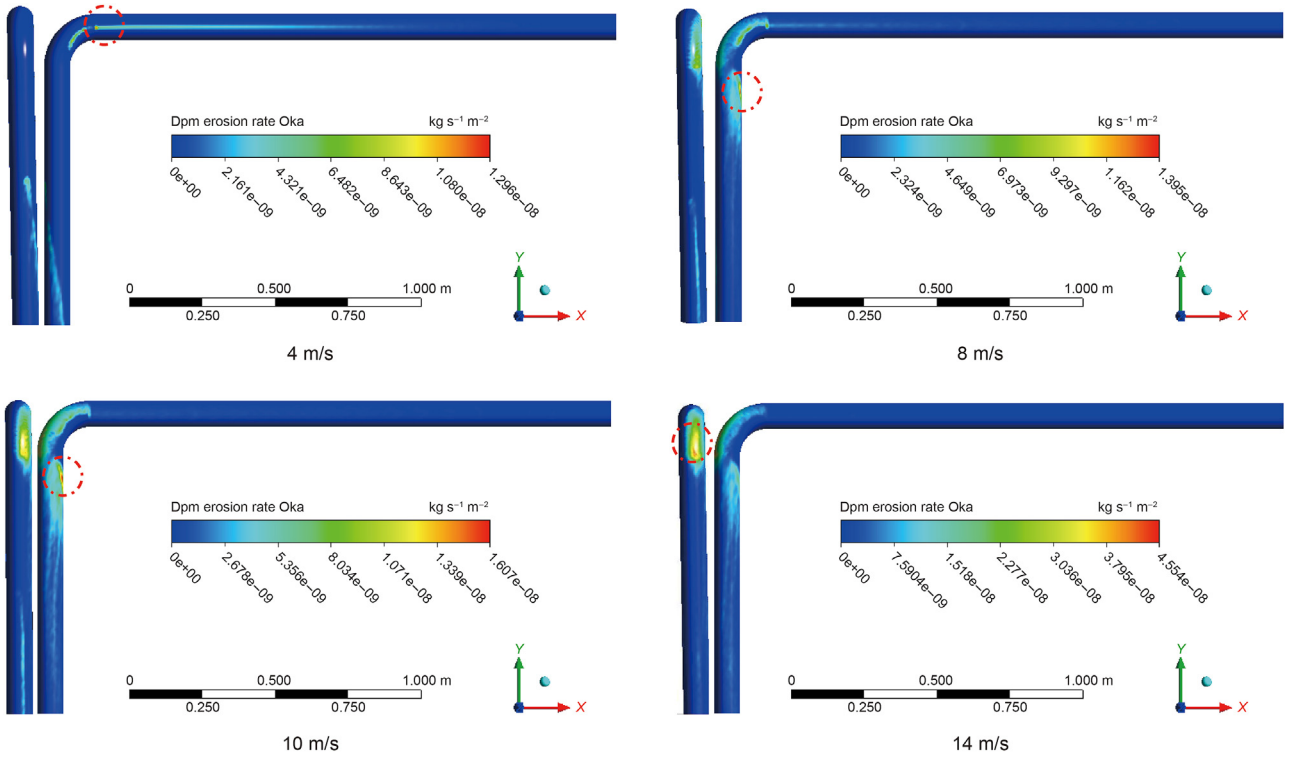

Fig. 11. Erosion cloud map of pipelines with different flow rates.

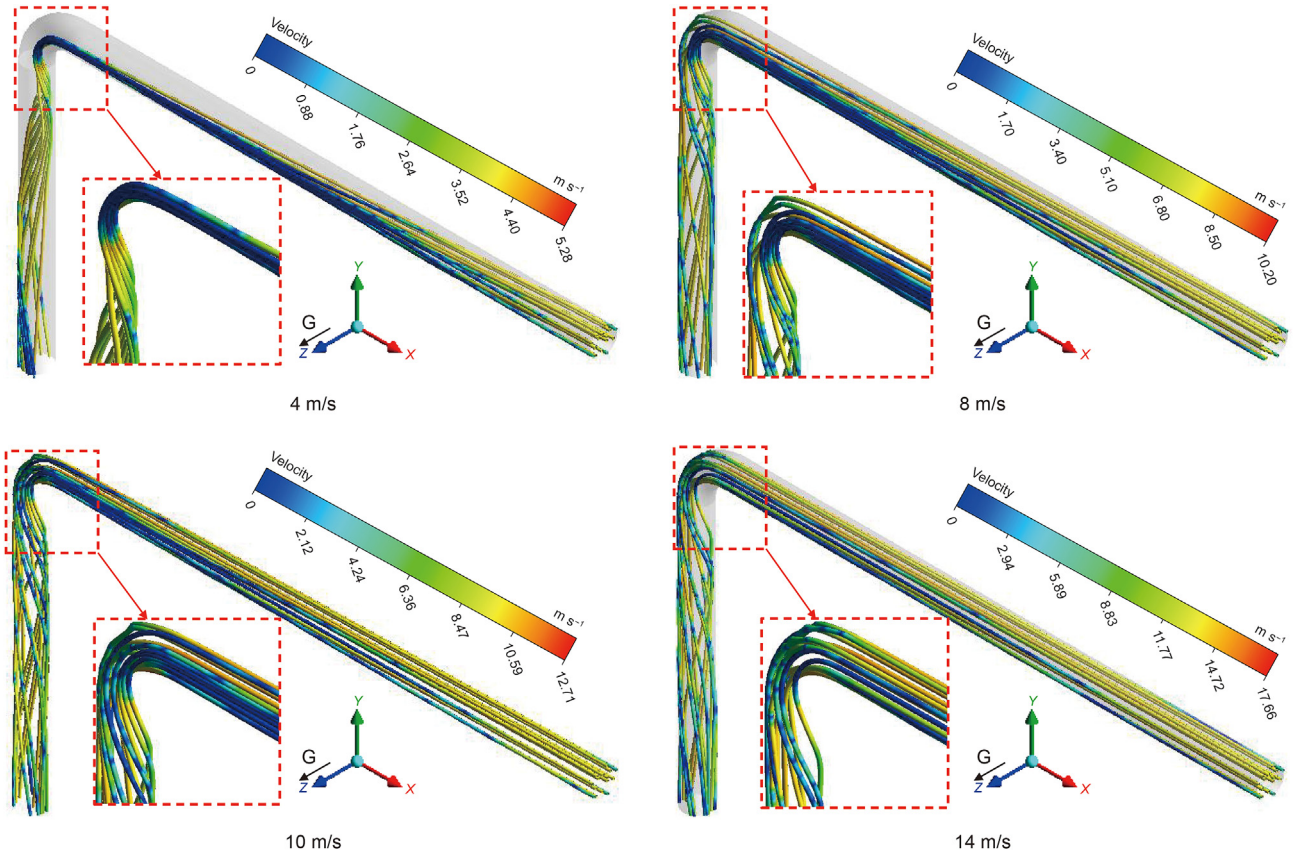

Fig. 12. Particle trajectory distribution at different flow rates.

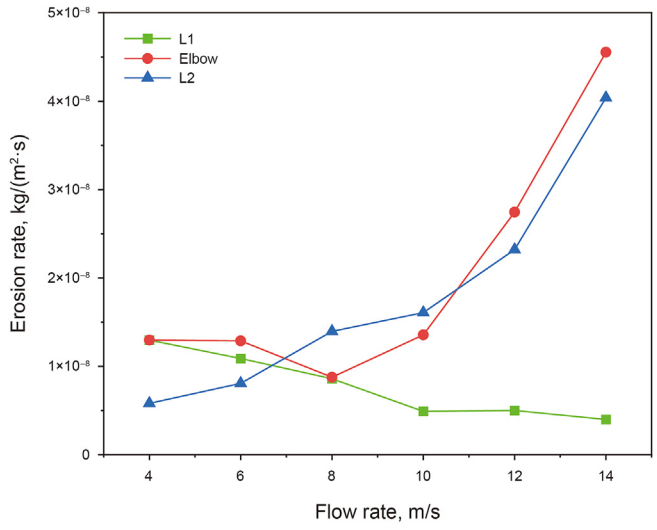

Fig. 13. Maximum erosion rate at different flow rates of each part of the pipeline.

on the cross-section R5–R8, and the erosion rate increases with the cross-section angle. The maximum erosion rate of 1.31 × 10^{-8} kg/(s·m^2) of cross-sections R1–R9 was detected in the area at 251° on section 9.

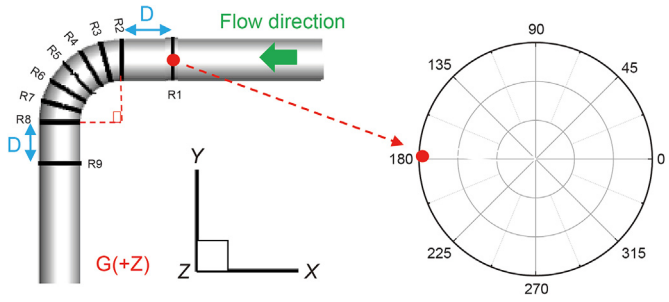

Fig. 14. Schematic diagram of the data lifting section.

3.2.2. *Influence of pressure on elbow erosion*

The flow field in the pipeline is simulated when the gathering and transportation pressure is 4–9 MPa, and the erosion behavior of particles in the pipeline is analyzed. Other parameters use the reference conditions.

Fig. 16 indicates that the maximum erosion rate decreases as the pressure increase. This is because the increase of pressure leads to the increase of shale gas density and viscosity, which increases the resistance of particles and reduces the contact between particles and the wall surface. When the pressure is low (4–7 MPa), the main erosion area is L2. As the pressure increases (8–9 MPa), the main erosion area shifts to the elbow, and relatively obvious marks of erosion occur at the outlet of the pipeline.

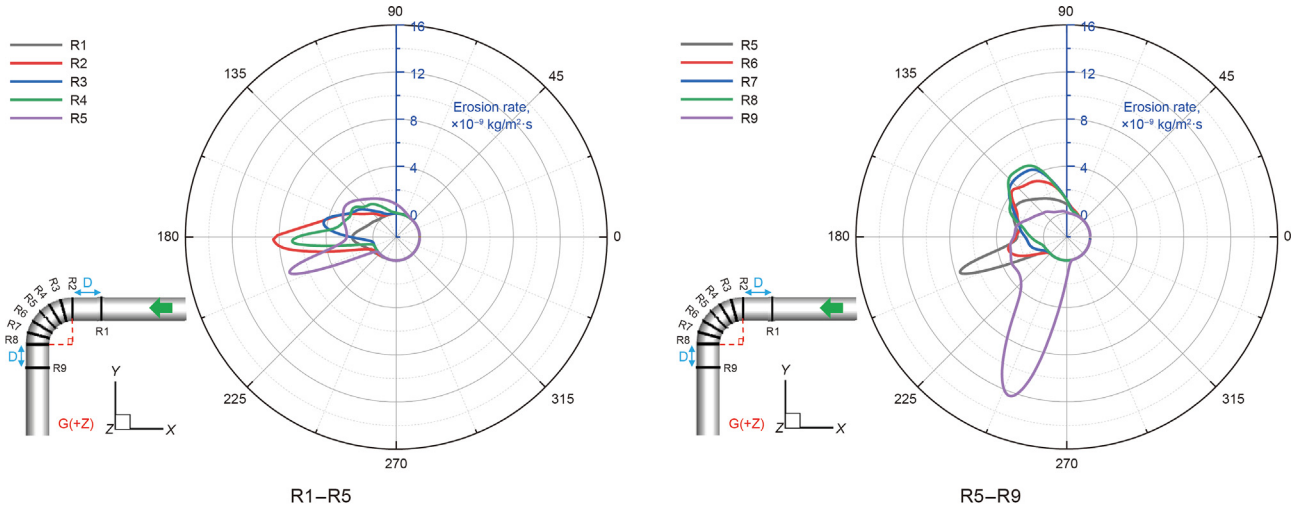

Fig. 15. Distribution curve of circumferential erosion on R1–R9 at 8 m/s.

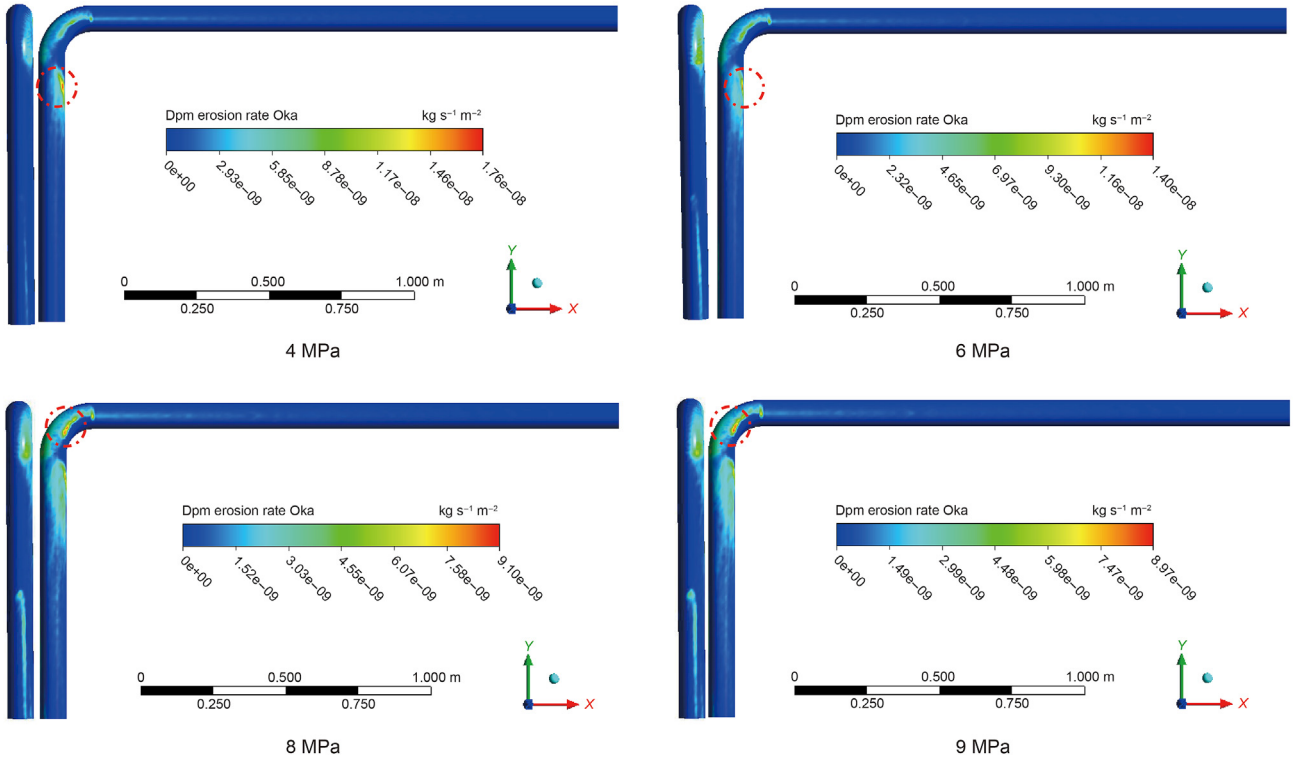

Fig. 16. Erosion cloud map of pipelines with different pressures.

As is shown in Fig. 17, the maximum erosion rate of each area of the gas-gathering pipeline decreases as the pressure increase. The erosion effect on L1 has always been relatively weak, and the erosion effect on the elbow area is slightly stronger than that on L1, but the erosion rates of both of them are very slow with the influence of pressure. L2 is seriously affected by erosion when the pressure is low, and the erosion rate decreases sharply as the pressure increase. Therefore, in the actual production process, the gas gathering pressure should be increased as much as possible to slow down the erosion effect on the entire pipeline.

Fig. 18 shows the erosion curves of the wall surface of the cross-section of elbows R1–R9 at the collector pressure of 7 MPa under the benchmark working condition. It can be seen from the figure that, compared with Fig. 12, as the pressure increases, the erosion rate on each section decreases, and the area with severe erosion and the position where the maximum erosion rate occurs remain unchanged. The erosion rate of the sections R5–R9 increases as the section angle increases, and the maximum erosion rate of the

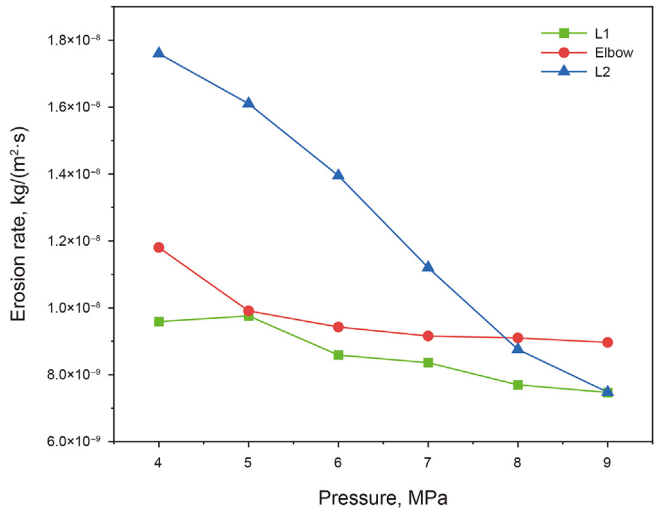

Fig. 17. Maximum erosion rate at different pressures of each part of the pipeline.

sections R1–R9 decreases to 1.03 × 10^{-8} kg/(s·m^2).

3.2.3. Influence of particle size on elbow erosion

The impact of single-particle size on the wall erosion of the gas gathering pipeline under the benchmark working condition is analyzed, and the particle size values are shown in Table 6.

As is shown in Fig. 19, the maximum erosion rate increases as the particle size increases. When the particle size is small (80, 96 μm), severe erosion occurs on the outer wall of the elbow. When the particle size gradually increases (125–212 μm), the erosion on the outer wall of the elbow is weakened, and the area with serious erosion changes to L2. When the particle size is 212 μm, the maximum erosion rate is 5.55 × 10^{-8} kg/(s·m^2).

Fig. 20 is the erosion curve diagram of the upper wall surface of the elbow R1–R9 section when the particle size is 150 μm under the reference working condition. It can be seen that the erosion rate of sections R1–R9 increases with the increase of section angle, and the maximum erosion rate is 2.94 × 10^{-8} kg/(s·m^2), which appears at 251° on section R9. The erosion areas are relatively concentrated on the sections, which are located at 150°–180° on sections R1–R3 and 90°–145° on sections R5–R8 respectively. The maximum erosion rate of sections R1–R5 is 9.52 × 10^{-9} kg/(s·m^2), which occurs on the area at 150° on section 5.

As is shown in Fig. 21, the erosion rate on L1 is basically not affected by the particle size. In the elbow area, when the particle size is less than 180 μm, the erosion rate increases linearly with the particle size, but the increase is small; when the particle size is larger than 180 μm, the erosion rate increases rapidly. The erosion rate of L2 takes on a linear increase and suffers from the most serious erosion. Therefore, in the actual production process, the separation efficiency of the desander should be improved to avoid large particles entering the gathering pipeline.

3.2.4. Influence of L1 length on elbow erosion

The erosion problem of elbows with different lengths of L1 was analyzed. The length of L1 is selected according to Table 6, and the other parameters are based on the benchmark working condition.

As is shown in Fig. 22, under the same simulation conditions, the main erosion areas are the same, both on the elbow and L2. The longer L1 is, the greater the erosion rate of the elbow, and the erosion area is more concentrated, which is shown as the deepening of the erosion "scar" in the figure. This is because as the straight section becomes longer, more and more particles settle to the bottom of the pipe and continue to slide, and as the length of the straight section of the inlet increases, so does the length of the erosion area.

Fig. 23 is the erosion curve diagram of the upper wall surface of the section of elbow R1–R9 under the benchmark working condition when the length of L1 is 30 D. It can be seen from the figure that in the sections R1–R5, the range of erosion angle corresponding to each section is nearly the same; and as the section angle increases, the erosion rate of the corresponding section increases, and the maximum rate is 1.49 × 10^{-8} kg/(s·m^2), occurring on the area at 196° on section R5. At this time, the erosion rate of sections R6–R8 is small, but that of section R9 is relatively large. This is because the particles are gradually separated from the wall

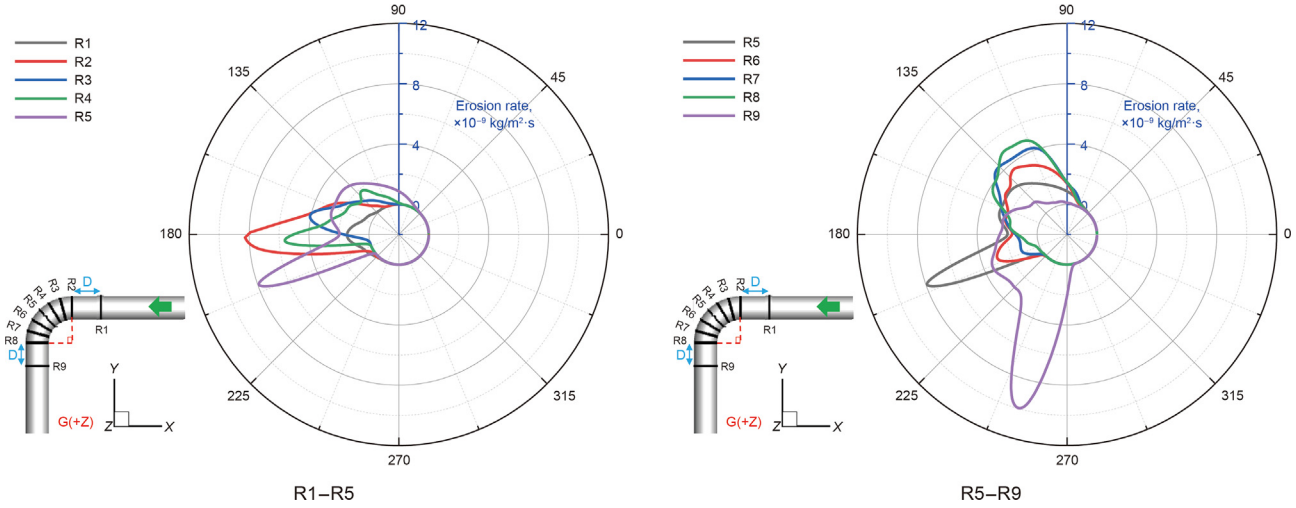

Fig. 18. Distribution curve of circumferential erosion on R1–R9 at 7 MPa.

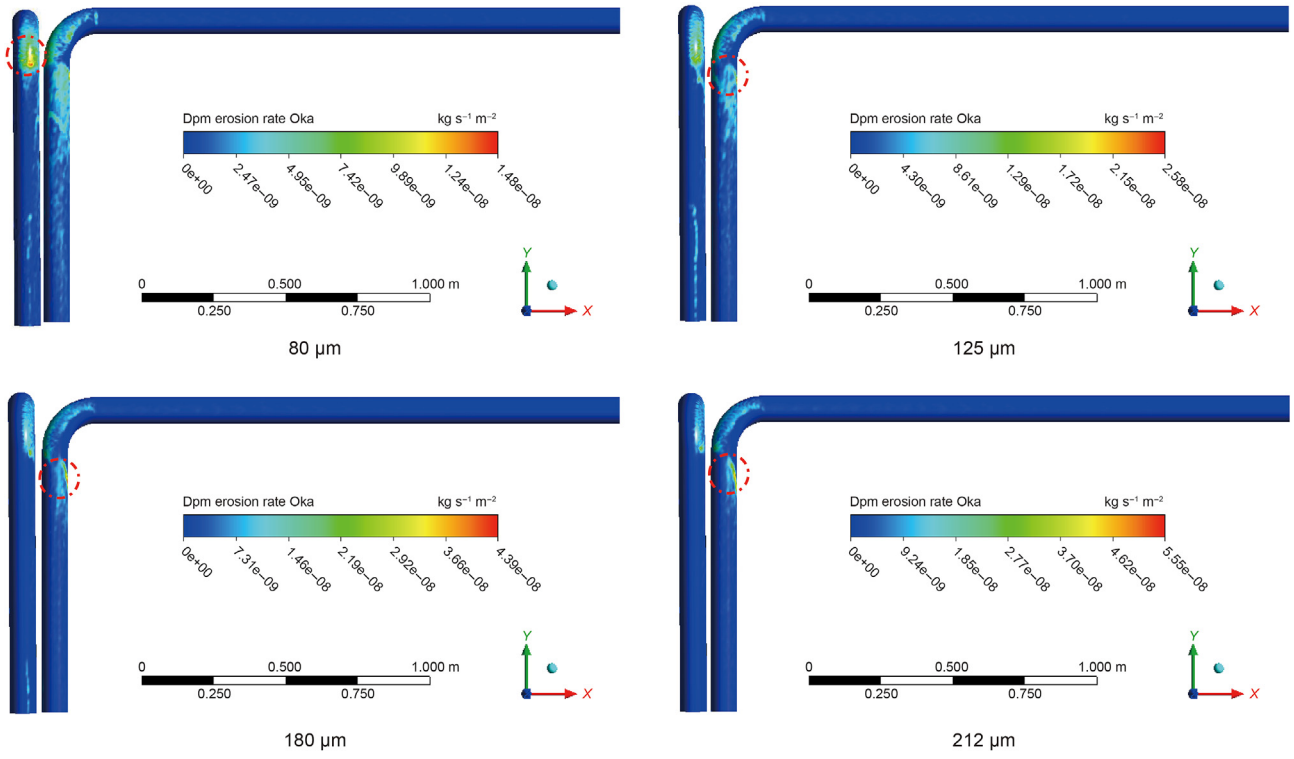

Fig. 19. Erosion cloud map of pipelines with different particle sizes.

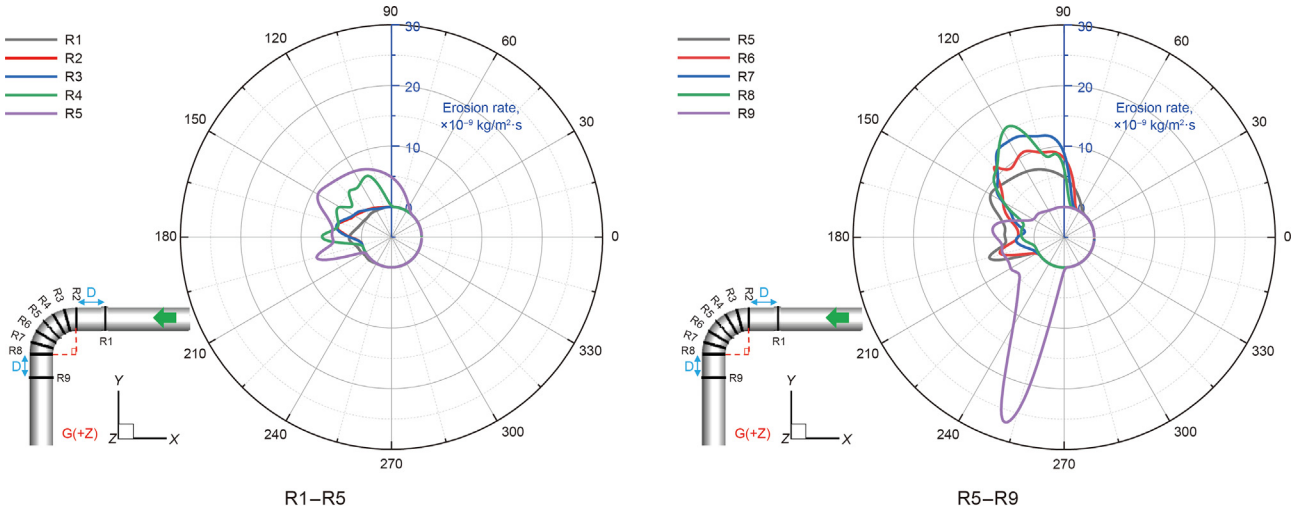

Fig. 20. Distribution curve of circumferential erosion on R1–R9.

by the centrifugal action and collide with L2, and the impact angle is large at this time.

Fig. 24 indicates that the erosion rate of the elbow increases with the length of the L1. When the length of L1 is 20 −35 D, the maximum erosion rate of the pipeline is 1.395×10^{-8}–4.762×10^{-8} kg/(s·m^2). Therefore, to reduce the erosion rate of the elbow, the length of L1 should be controlled within an appropriate range.

3.2.5. *Influence of bending direction on elbow erosion*

The influence of different bending directions on elbow erosion was analyzed. The particle erosion behavior when the gravity direction was +Y, −Y, +Z was simulated, and the other parameters were based on the benchmark working conditions.

As can be seen from Figs. 25 and 26, when the gravity direction is −Y, particle tracks are most concentrated and impact the pipe wall with parabolic motion. At this time, the impact angle is large, resulting in concentrated erosion area at L2 and superposition of

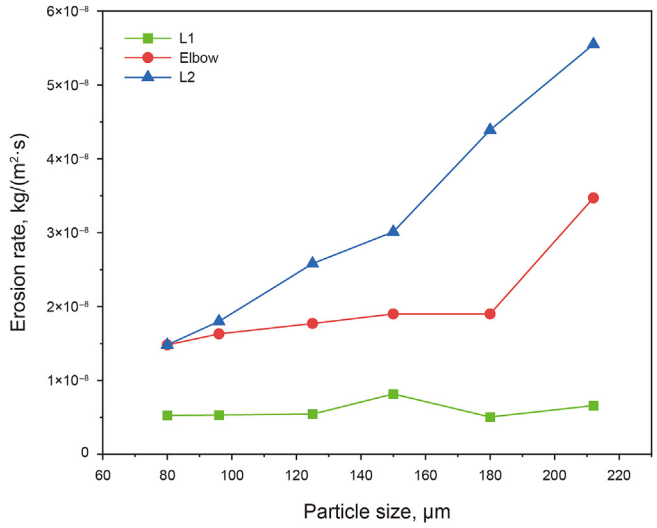

Fig. 21. Maximum erosion rate at different particle sizes in each part of the pipeline.

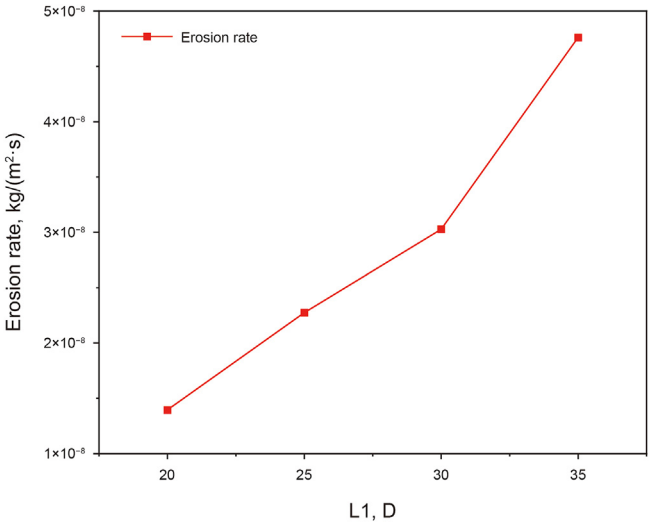

Fig. 24. Maximum erosion rate at different lengths of L1.

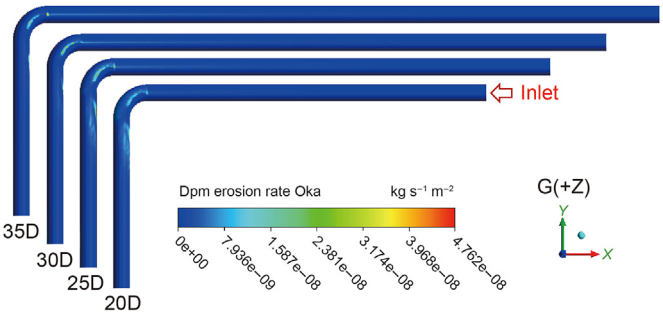

Fig. 22. Erosion rate of pipelines with different lengths of L1.

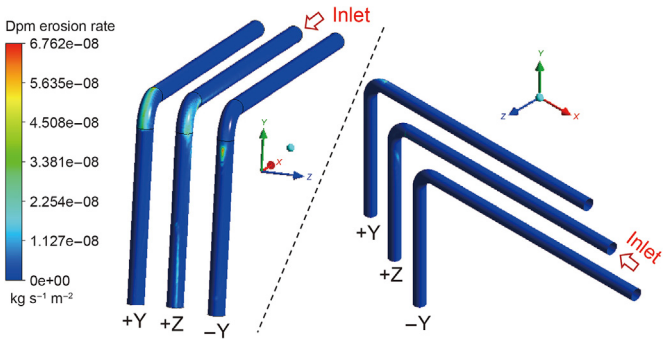

Fig. 25. Erosion cloud map of the elbow in different bending directions.

erosion effect, so the erosion rate reaches the maximum, 6.762 × 10^{-8} kg/(s·m^2). When the gravity direction is +Y, the particles move along the pipe wall under the action of gravity, and the erosion is concentrated on the elbow wall. The maximum erosion rate is 2.260 × 10^{-8} kg/(s·m^2). When the gravity direction is +Z, the particle aggregation degree is low, so the erosion rate is relatively small. The main erosion area is located on the elbow wall,

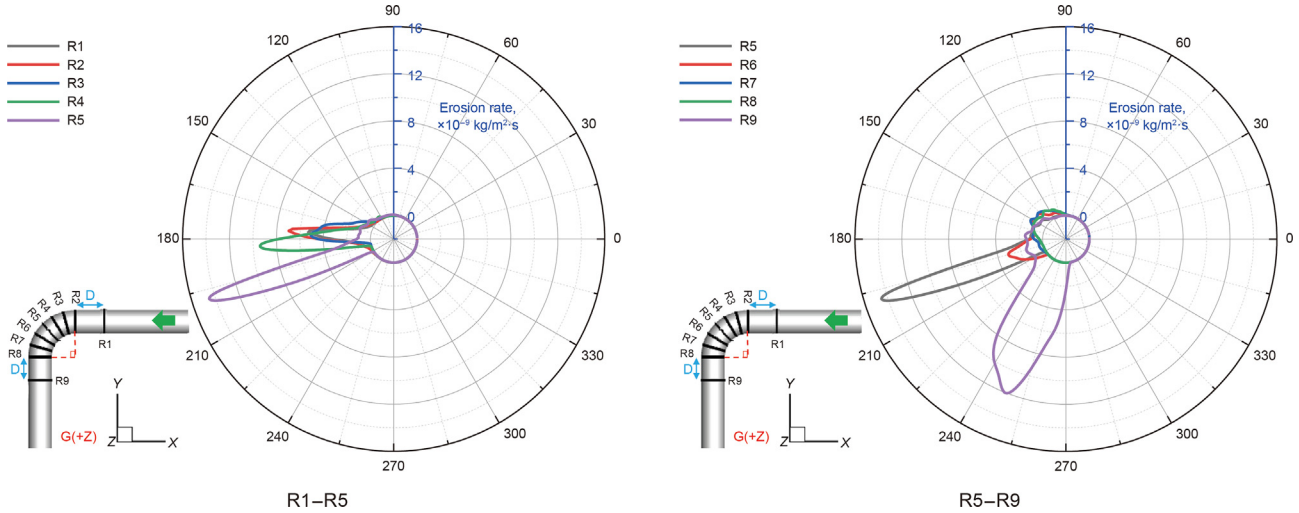

Fig. 23. Distribution curve of circumferential erosion on R1–R9.

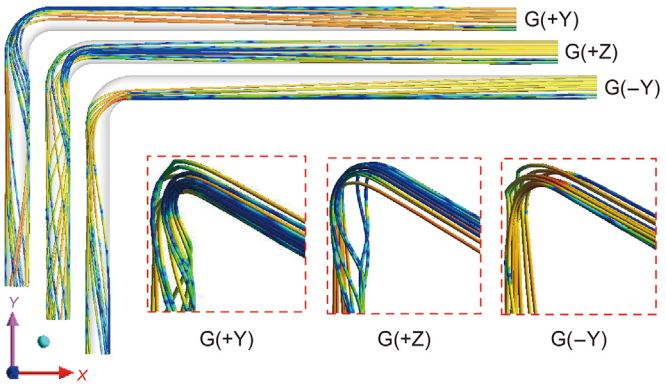

Fig. 26. Particle trajectory distribution in different bending directions.

and the maximum erosion rate is 1.395 × 10^{-8} kg/(s·m^2). Compared to the elbow with gravity direction +Z, the maximum erosion rate increases by 88% and 385% for gravity direction +Y and −Y, respectively.

Fig. 27(a)–(d) are the circumferential erosion distribution curves in the +Y and −Y gravity directions, respectively. As is shown in the figure, data are extracted from seven sections on the elbow wall and six sections on the wall of L2 respectively.

Combined with the particle trajectory diagram, it can be seen that the range of erosion angles on the cross-section is relatively concentrated in both working conditions, which are located at 60°–90° and 86°–95° respectively, and the maximum erosion rate occurs at 90°. The difference is that the maximum erosion rate in the +Y gravity direction appears on section R1, the erosion rate on sections R1 to R4 decreases as the section angle increase, and the maximum erosion rate on sections R4 to R7 is nearly the same;

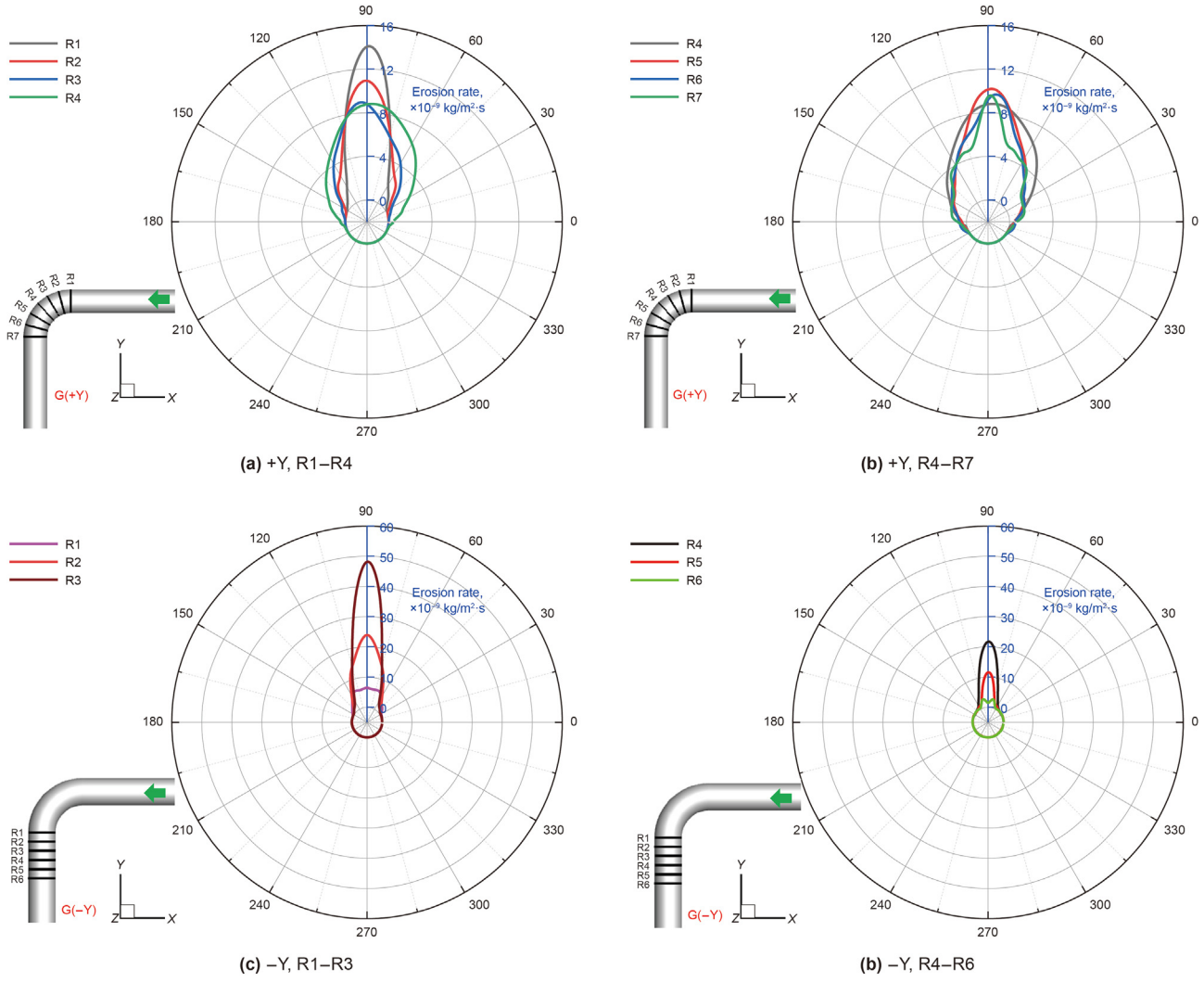

Fig. 27. Distribution curves of circumferential erosion in +Y and −Y gravity directions.

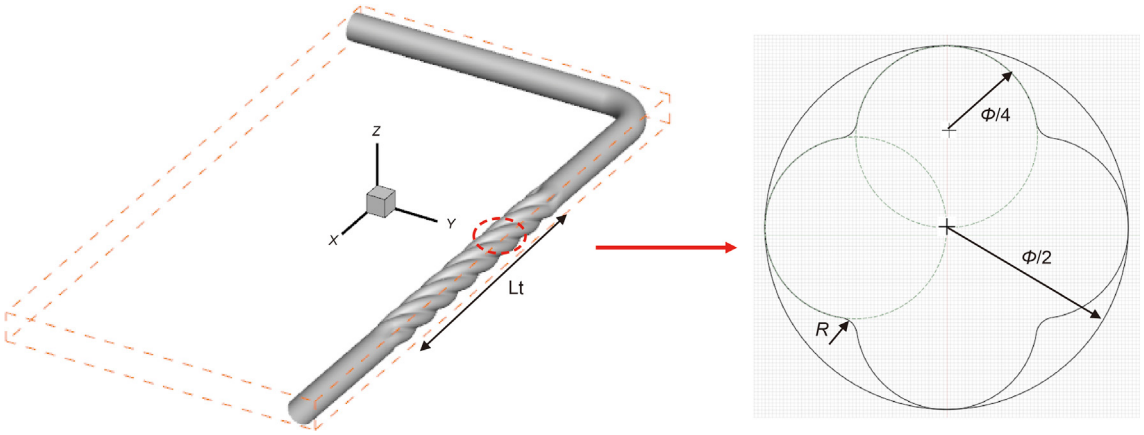

Fig. 28. Schematic diagram of the spiral tube structure.

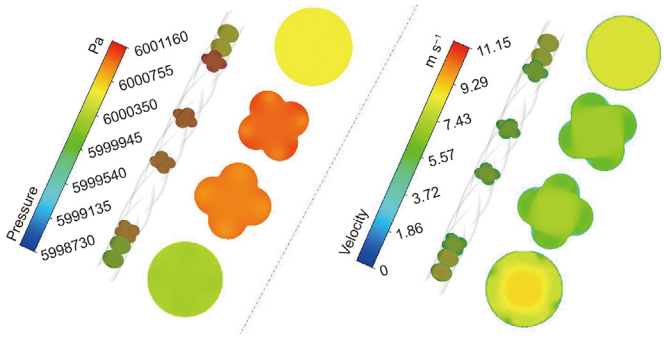

Fig. 29. Cloud map of pressure and velocity of the spiral pipe.

when the direction of gravity is −Y, the maximum erosion rate appears on section R3, the erosion rate on sections R1–R3 increases with the section angle, and the erosion rate on sections R4–R6 gradually becomes smaller.

3.3. Mitigation solution for elbow erosion

3.3.1. Spiral tube structure

From the study in the previous section, it was found that the degree and speed of particle aggregation have a great influence on the erosion rate and the distribution of the erosion area in the elbow. Therefore, this paper proposes an internal spiral tube structure that can be used for shale gas gathering based on the previous study (Duarte and Souza, 2017). The difference from previous studies is that the threads of the structure in this paper are located on the inner wall surface of the pipe, and the outer wall surface is kept smooth. This not only reduces the degree of particle aggregation by changing the particle flow direction, but also increases the flow area and reduces the fluid flow rate in the pipe, thus achieving effective control of the elbow erosion rate.

As is shown in Fig. 28, a section of spiral pipe with the length of Lt = 15 D is added before horizontally placing the elbow, whose cross-section mainly consists of four circles, which can be regarded as a circle rotated by a certain angle three times in succession around the center of the common circumscribed circle of the four circles, and the redundant part is deleted. The diameter of the common circumscribed circle is ϕ, and the flow area of the spiral pipe section is $(2+\pi)\phi^2/8$.

3.3.2. Influence of spiral pipe diameter on elbow erosion

This paper studies the erosion of the elbow when the flow area of the spiral pipe section is 1.0, 1.2, and 1.5 times the flow area of the conventional pipe section, corresponding to the circumscribed circle diameters of the spiral pipe section of 98.4, 107.8 and 120.5 mm. The remaining parameters in the pipe wall design take the recommended values from the literature (Duarte and Souza, 2017): the number of small circles is 4, the diameter ratio of large and small circles is 2:1, the pitch is 1000 mm, and the radius of the smooth connection section is $R = 5$ mm.

Fig. 29 shows the pressure and velocity cloud diagrams of the spiral pipe with 1.2 times the flow area under the benchmark working condition. It indicates that the maximum pressure difference in the spiral pipe section is 2430 Pa, and the airflow velocity is between 6–7 m/s, which is significantly lower than that in the conventional pipe.

Fig. 30 shows the erosion cloud diagrams of the 1.0A, 1.2A, and 1.5A spiral pipe sections, respectively. It indicates that the maximum erosion rates of the 1.0A, 1.2A, and 1.5A pipe sections are 1.396×10^{-8}, 1.241×10^{-8} and 9.283×10^{-9} kg/(s·m^2), and the areas with maximum erosion are both located in the elbow. The maximum erosion rate of the 1.0A pipe section is the same as that of the conventional pipe section. The maximum erosion rate of the 1.2A and 1.5A pipe sections is 11% and 34% lower than that of the conventional pipe section, respectively.

Fig. 31 is a graph of particle trajectories of conventional pipe sections and 1.0A, 1.2A, and 1.5A helical pipe sections. It can be seen that the degree of aggregation of the particles is significantly reduced after adding the spiral tube section. When the 1.5A spiral pipe section is added, the particles in the entire pipeline are most widely distributed on the cross-section of the flow direction, and the degree of aggregation is the lowest, thus avoiding concentrated erosion and greatly reducing the maximum erosion rate of the pipeline.

Fig. 32 shows the radar map of the erosion rate at three parts of the pipeline. It can be seen that the conventional pipe section presents an acute triangle. When the spiral pipe section is added, the minimum angle of the triangle presented by 1.0A, 1.2A, and 1.5A

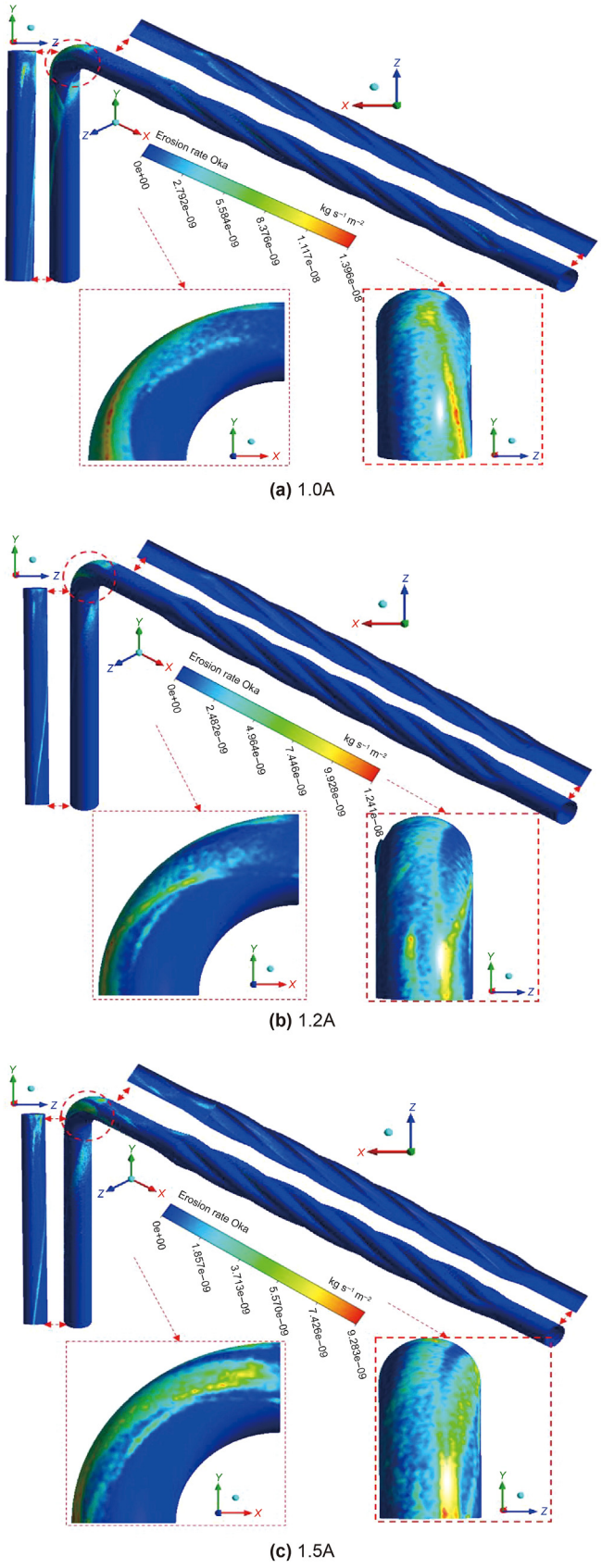

Fig. 30. Erosion cloud map of the spiral pipe.

in the radar chart gradually increases, that is, the maximum erosion rate of the pipeline gradually decreases. At 1.5A, the triangle is nearly a the equilateral triangle, and the maximum erosion rates of the three parts are the same, which shows that the spiral pipe section can balance the gap between the erosion rates of L1 and L2 and the elbow, reduce the maximum erosion rate of the whole pipeline, and improve the safety of the pipeline.

This scheme has the following advantages: 1) Only a part of the pipe section needs to be replaced without affecting the structural integrity and continuity of the original pipe section; 2) The structural inspection and maintenance of the spiral pipe section is no different from that of conventional pipes; 3) This scheme can coexist with other corrosion inhibition measures.

4. Conclusion

(1) According to the experimental results of gas-solid two-phase erosion, it is found that the elbow at different angles has different material removal mechanisms and erosion rates (Peng et al., 2021a) and the maximum erosion rate occurs at about 60° of the elbow. By numerically simulating the experimental pipe section and then comparing the experimental results, it is found that the Oka model agrees well with the experimental results, and the relative error of the areas with high erosion rate is controlled within the range of −11% to +18%, with high prediction accuracy (Peng et al., 2021b; Qiao et al., 2021a).

(2) By analyzing the influence of different parameters on elbow erosion, it is found that the erosion rate increases with the gas flow rate, particle size, and the length of L1, and decreases with the increase of gas gathering pressure. In the case of different elbow bending directions, the maximum erosion rate increases by 88% and 385% for the gravity direction +Y and −Y, respectively, compared to the pipeline with gravity direction +Z. And the region where the maximum erosion rate occurs varies with the above parameters (Qiao et al., 2021b). After a comprehensive comparison of various factors, it was found that gas flow rate and particle aggregation degree are the main factors affecting the erosion rate and distribution of erosion areas of elbows.

(3) This paper proposes an internal spiral tube structure to reduce the erosion rate for the elbow. Through simulation analysis, the maximum erosion rate of the elbow after adding the 1.2A and 1.5 A spiral pipe sections decreased by 11% and 34% respectively compared with that of conventional pipe sections.

The discovery of this work is helpful to alleviate the erosion situation of gathering and transportation pipelines in the Changning Shale Gas Field. The prediction of elbow erosion rate and erosion area distribution according to the field working conditions is of great significance. However, the relative error between the prediction results of the prediction model and the experimental results in the area of 0°–40° of the elbow is still large. Therefore, in order to obtain more accurate prediction results, it is suggested to establish a more accurate erosion prediction model based on big data, artificial intelligence and other methods according to the actual field conditions.

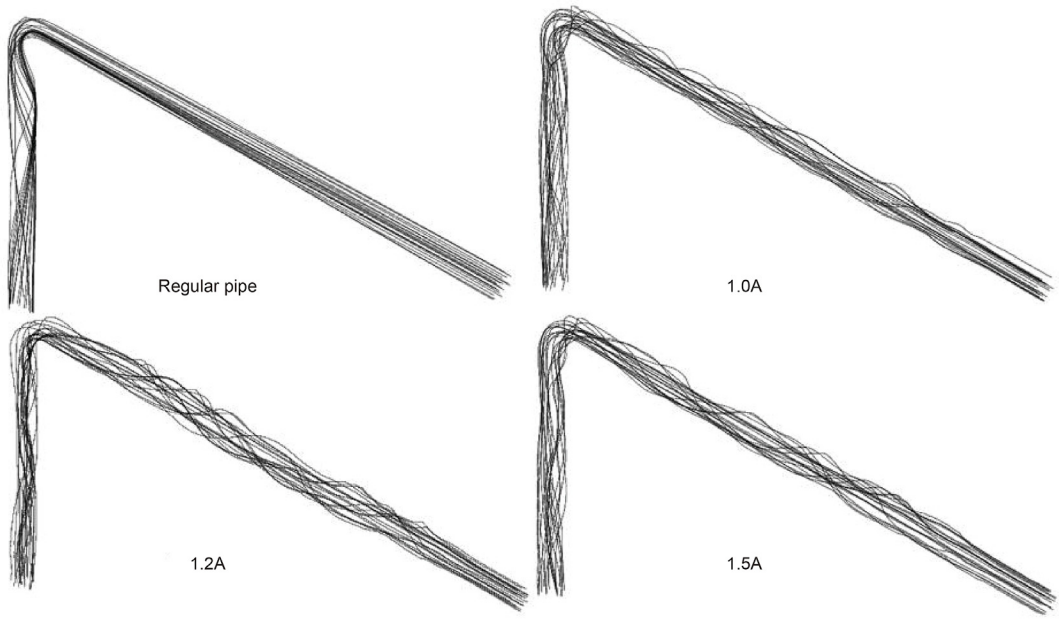

Fig. 31. Particle trajectory diagram of the spiral pipe section.

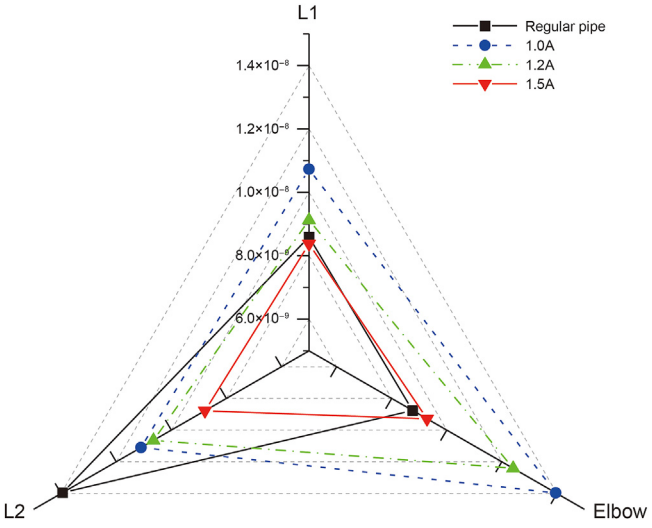

Fig. 32. Erosion rate radar map of each part of the pipeline.

Declaration of competing interest

The authors declare that they have no known competing financial interests or personal relationships that could have appeared to influence the work reported in this paper.

Acknowledgments

This work was supported by the Petrochina's "14th Five-Year plan" Project (2021DJ2804) and Sichuan Natural Science Foundation (2023NSFSC0422).

References

Arabnejad, H., Shirazi, S.A., McLaury, B.S., et al., 2015. The effect of erodent particle hardness on the erosion of stainless steel. Wear 332, 1098–1103. https://doi.org/10.1016/j.wear.2015.01.017.

Chen, Y., Fu, W., Deng, H., 2020. Central tube erosion investigation of torque impactor in the deep shale gas formation. Energy Sources, Part A Recovery, Util. Environ. Eff. 1–15. https://doi.org/10.1080/15567036.2020.1732504.

Duarte, C.A.R., de Souza, F.J., 2017. Innovative pipe wall design to mitigate elbow erosion: a CFD analysis. Wear 380, 176–190. https://doi.org/10.1016/j.wear.2017.03.015.

Forder, A., Thew, M., Harrison, D., 1998. A numerical investigation of solid particle erosion experienced within oilfield control valves. Wear 216 (2), 184–193. https://doi.org/10.1016/S0043-1648(97)00217-2.

Fu, Y., Wang, J., 2015. Experimental and computational failure analysis of flow erosion on new throttle in gas drilling. Petroleum & Coal 57 (3), 246–252. https://doi.org/10.1016/j.engfailanal.2011.09.004.

Farokhipour, A., Mansoori, Z., Rasteh, A., et al., 2019. Study of erosion prediction of turbulent gas-solid flow in plugged tees via CFD-DEM. Powder Technol. 352, 136–150. https://doi.org/10.1016/j.powtec.2019.04.058.

Grant, G., Tabakoff, W., 1975. Erosion prediction in turbomachinery resulting from environmental solid particles. J. Aircraft. 12 (5), 471–478. https://doi.org/10.2514/3.59826.

Haider, A., Levenspiel, O., 1989. Drag coefficient and terminal velocity of spherical and nonspherical particles. Powder Technol. 58 (1), 63–70. https://doi.org/10.1016/0032-5910(89)80008-7.

Hong, B., Li, Y., Li, X., et al., 2022. Experimental investigation of erosion rate for gas-solid two-phase flow in 304 stainless/L245 carbon steel. Petrol. Sci. 19 (3), 1347–1360. https://doi.org/10.1016/j.petsci.2022.01.011.

Islam, M.A., Alam, T., Farhat, Z., 2016. Construction of erosion mechanism maps for pipeline steels. Tribol. Int. 102, 161–173. https://doi.org/10.1016/j.triboint.2016.05.033.

Jassim, E., Abdi, M.A., Muzychka, Y., 2010. A new approach to investigate hydrate deposition in gas-dominated flowlines. J. Nat. Gas Sci. Eng. 2 (4), 163–177. https://doi.org/10.1016/j.jngse.2010.05.005.

Khan, R., Ya, H.H., Pao, W., 2019. An experimental study on the erosion-corrosion performance of AISI 1018 carbon steel and AISI 304L stainless steel 90-degree elbow pipe. Metals 9 (12), 1260. https://doi.org/10.3390/met9121260.

Levy, A.V., 1981. The solid particle erosion behavior of steel as a function of microstructure. Wear 68 (3), 269–287. https://doi.org/10.1016/0043-1648(81)90177-0.

Liu, E., Lv, L., Yi, Y., et al., 2019. Research on the steady operation optimization model of natural gas pipeline considering the combined operation of air coolers and compressors. IEEE Access 7, 83251–83265. https://doi.org/10.1109/ACCESS.2019.2924515.

Liu, E., Li, D., Li, W., et al., 2021a. Erosion simulation and improvement scheme of separator blowdown system-A case study of Changning national shale gas demonstration area. J. Nat. Gas Sci. Eng. 88, 103856. https://doi.org/10.1016/j.jngse.2021.103856.

Liu, E., Wang, X., Zhao, W., et al., 2021b. Analysis and research on pipeline vibration of a natural gas compressor station and vibration reduction measures. Energy Fuel. 35 (1), 479–492. https://doi.org/10.1021/acs.energyfuels.0c03663.

Nguyen, Q.B., Nguyen, V.B., Lim, C.Y.H., et al., 2014. Effect of impact angle and testing time on erosion of stainless steel at higher velocities. Wear 321, 87–93. https://doi.org/10.1016/j.wear.2014.10.010.

Oka, Y.I., Nagahashi, K., 2003. Measurements of plastic strain around indentations caused by the impact of round and angular particles, and the origin of erosion. Wear 254 (12), 1267–1275. https://doi.org/10.1016/S0043-1648(03)00048-6.

Oka, Y.I., Yoshida, T., 2005. Practical estimation of erosion damage caused by solid particle impact: Part 2: mechanical properties of materials directly associated with erosion damage. Wear 259 (1–6), 102–109. https://doi.org/10.1016/j.wear.2005.01.040.

Pagalthivarthi, K.V., Gupta, P.K., Tyagi, V., et al., 2011. CFD prediction of erosion wear in centrifugal slurry pumps for dilute slurry flows. J. Comput. Multiph. Flows. 3 (4), 225–245. https://doi.org/10.1260/1757-482X.3.4.225.

Parvaz, F., Hosseini, S.H., Elsayed, K., et al., 2018. Numerical investigation of effects of inner cone on flow field, performance and erosion rate of cyclone separators. Separ. Purif. Technol. 201, 223–237. https://doi.org/10.1016/j.seppur.2018.03.001.

Peng, S., Chen, Q., Shan, C., et al., 2019. Numerical analysis of particle erosion in the rectifying plate system during shale gas extraction. Energy Sci. Eng. 7 (5), 1838–1851. https://doi.org/10.1002/ese3.395.

Peng, S., Chen, Q., Zheng, C., et al., 2020a. Analysis of particle deposition in a new-type rectifying plate system during shale gas extraction. Energy Sci. Eng. 8 (3), 702–717. https://doi.org/10.1002/ese3.543.

Peng, S., Chen, Q., Liu, E., 2020b. The role of computational fluid dynamics tools on investigation of pathogen transmission: prevention and control. Sci. Total Environ. 746, 142090. https://doi.org/10.1016/j.scitotenv.2020.142090.

Peng, S., Chen, R., Yu, B., et al., 2021a. Daily natural gas load forecasting based on the combination of long short term memory, local mean decomposition, and wavelet threshold denoising algorithm. J. Nat. Gas Sci. Eng. 95, 104175. https://doi.org/10.1016/j.jngse.2021.104175.

Peng, S., Zhang, Z., Liu, E., et al., 2021b. A new hybrid algorithm model for prediction of internal corrosion rate of multiphase pipeline. J. Nat. Gas Sci. Eng. 85, 103716. https://doi.org/10.1016/j.jngse.2020.103716.

Qiao, W., Liu, W., Liu, E., 2021a. A combination model based on wavelet transform for predicting the difference between monthly natural gas production and consumption of US. Energy 235, 121216. https://doi.org/10.1016/j.energy.2021.121216.

Qiao, W., Wang, Y., Zhang, J., et al., 2021b. An innovative coupled model in view of wavelet transform for predicting short-term PM10 concentration. J. Environ. Manag. 289, 112438. https://doi.org/10.1016/j.jenvman.2021.112438.

Rodriguez, E., Flores, M., Pérez, A., et al., 2009. Erosive wear by silica sand on AISI H13 and 4140 steels. Wear 267 (11), 2109–2115. https://doi.org/10.1016/j.wear.2009.08.009.

Sun, X.Y., Cao, X.W., 2021. Impact of inter-particle collision on elbow erosion based on DSMC-CFD method. Petrol. Sci. 18, 909–922. https://doi.org/10.1007/s12182-021-00550-5.

Tofighian, H., Amani, E., Saffar-Avval, M., 2020. A large eddy simulation study of cyclones: the effect of sub-models on efficiency and erosion prediction. Powder Technol. 360, 1237–1252. https://doi.org/10.1016/j.powtec.2019.10.091.

Yabuki, A., Matsuwaki, K., Matsumura, M., 1999. Critical impact velocity in the solid particles impact erosion of metallic materials. Wear 233, 468–475. https://doi.org/10.1016/S0043-1648(99)00170-2.

Yang, S., Zhang, L., Fan, J., et al., 2021. Experimental study on erosion behavior of fracturing pipeline involving tensile stress and erosion prediction using random forest regression. J. Nat. Gas Sci. Eng. 87, 103760. https://doi.org/10.1016/j.jngse.2020.103760.

Yi, J., He, S., Wang, Z., et al., 2021. Effect of impact angle on the critical flow velocity for erosion–corrosion of 304 stainless steel in simulated sand-containing sea water. J. Bio. Tribo-Corrosion 7 (3), 1–9. https://doi.org/10.1007/s40735-021-00538-z.

Zhang, Y., McLaury, B.S., Shirazi, S.A., 2009. Improvements of particle near-wall velocity and erosion predictions using a commercial CFD code. J. Fluid Eng. 131 (3), 031303. https://doi.org/10.1115/1.3077139.

Zhang, X., Liu, W., Jiang, D., et al., 2021. Investigation on the influences of interlayer contents on stability and usability of energy storage caverns in bedded rock salt. Energy 231, 120968. https://doi.org/10.1016/j.energy.2021.120968.